

Kaonic production of $\Lambda(1405)$ off deuteron target in chiral dynamics

D. Jido,¹ E. Oset,² and T. Sekihara³

¹*Yukawa Institute for Theoretical Physics, Kyoto University, Kyoto 606-8502, Japan*

²*Departamento de Física Teórica and IFIC, Centro Mixto Universidad de Valencia-CSIC, Institutos de Investigación de Paterna, Aptdo. 22085, 46071 Valencia, Spain*

³*Department of Physics, Graduate School of Science, Kyoto University, Kyoto, 606-8502, Japan*

(Dated: June 21, 2024)

The K^- induced production of $\Lambda(1405)$ is investigated in $K^-d \rightarrow \pi\Sigma n$ reactions based on coupled-channels chiral dynamics, in order to discuss the resonance position of the $\Lambda(1405)$ in the $\bar{K}N$ channel. We find that the $K^-d \rightarrow \Lambda(1405)n$ process favors the production of $\Lambda(1405)$ initiated by the $\bar{K}N$ channel. The present approach indicates that the $\Lambda(1405)$ resonance position is 1420 MeV rather than 1405 MeV in the $\pi\Sigma$ invariant mass spectra of $K^-d \rightarrow \pi\Sigma n$ reactions. This is consistent with an observed spectrum of the $K^-d \rightarrow \pi^+\Sigma^-n$ with 686-844 MeV/c incident K^- by bubble chamber experiments done in the 70's. Our model also reproduces the measured $\Lambda(1405)$ production cross section.

PACS numbers: 14.20.Jn, 25.80.Nv, 13.75.Jz, 12.39.Fe; 13.30.Eg

Keywords: Structure of $\Lambda(1405)$; Kaon induced production of $\Lambda(1405)$; Chiral unitary model

I. INTRODUCTION

The structure of the $\Lambda(1405)$ resonance is an important recent issue particularly to understand \bar{K} -nucleus interactions. The $\Lambda(1405)$ has been a historical example of a dynamically generated resonance in meson-baryon coupled-channels dynamics with $S = -1$ [1]. Modern investigations based on chiral dynamics with a unitary framework also reproduce well the observed spectrum of the $\Lambda(1405)$ together with cross sections of K^-p to various channels [2, 3, 4, 5, 6, 7]. Recently it was pointed out in Ref. [8] that the $\Lambda(1405)$ can be regarded almost purely as a dynamically generated state in meson-baryon scattering, while the description of the $N(1535)$ demands some components other than meson-baryon ones, such as genuine quark components.

One of the important consequences of chiral dynamics is that the $\Lambda(1405)$ is described by superposition of two resonance states [9]. One state located around 1420 MeV couples dominantly to the $\bar{K}N$ channel, while the other one sitting around 1390 MeV with a 130 MeV width couples strongly to the $\pi\Sigma$ channel. Consequently, the spectra of the $\Lambda(1405)$ depend on the channels and the resonance position in the $\bar{K}N$ channel is 1420 MeV, higher than the nominal one which is 1405 MeV. Therefore, it is important to observe the resonance position of the $\Lambda(1405)$ in the $\bar{K}N$ channel.

To observe the resonance position of the $\Lambda(1405)$ in the $\bar{K}N$ channel it is necessary to produce the $\Lambda(1405)$ by reactions initiated by $\bar{K}N$. Since the $\Lambda(1405)$ resonance appears below the threshold of the $\bar{K}N$ channel, direct production of $\Lambda(1405)$ in the $\bar{K}N$ channel is kinematically forbidden. This fact leads us to indirect productions of $\Lambda(1405)$, such as $\gamma p \rightarrow \Lambda(1405)K^*$ [10], $K^-p \rightarrow \gamma\Lambda(1405)$ [11], $K^-p \rightarrow \pi_0\Lambda(1405)$ [12, 13], and nuclear reactions. Here we discuss the K^- induced production of $\Lambda(1405)$ with a deuteron target, $K^-d \rightarrow \Lambda(1405)n$. In this reaction, the final neutron takes energy out from

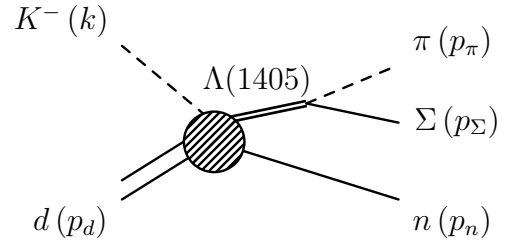


FIG. 1: Kinematics of the $K^-d \rightarrow \pi\Sigma n$.

the initial kaon and the $\Lambda(1405)$ is produced by the $\bar{K}N$ channel.

The paper is organized as follows: In Sec. II, we explain our model to calculate the $K^-d \rightarrow \pi\Sigma n$ reactions and introduce the description of $\Lambda(1405)$ based on the chiral unitary approach. In Sec. III we show our numerical results of the calculations and compare our results with experiments. Section IV is devoted to a summary of this work.

II. FORMULATION

In this section, we explain our approach to calculate the cross section of the $K^-d \rightarrow \pi\Sigma n$ reaction. In Sec. II A, we discuss the kinematics of this reaction and introduce relevant diagrams for the $\Lambda(1405)$ production. The T -matrix is calculated in Sec. II B. The description of the two-body meson-baryon scattering amplitudes and the model of $\Lambda(1405)$ in the chiral unitary approach are discussed in Sec. II C.

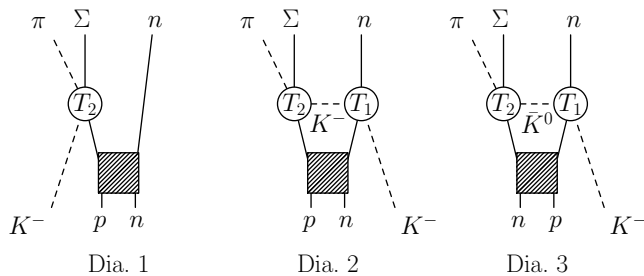


FIG. 2: Diagrams for the calculation of the $K^-d \rightarrow \pi\Sigma n$ reaction. T_1 and T_2 denote the scattering amplitudes for $\bar{K}N \rightarrow \bar{K}N$ and $\bar{K}N \rightarrow \pi\Sigma$, respectively.

A. Kinematics

We consider $\Lambda(1405)$ production induced by K^- with a deuteron target, $K^-d \rightarrow \Lambda(1405)n$. The $\Lambda(1405)$ produced in this reaction decays into $\pi\Sigma$ with $I = 0$ as shown in Fig. 1. The $\Lambda(1405)$ is identified by the $\pi\Sigma$ invariant mass spectra of this reaction. Figure 1 also gives the kinematical variables of the initial and final particles. The kinematics of the three-body final state is completely fixed by five variables, the $\pi\Sigma$ invariant mass $M_{\pi\Sigma}$, the neutron solid angle Ω_n in the c.m. frame and the pion solid angle Ω_π^* in the rest frame of π and Σ [14]. Thus the differential cross section of this reaction can be written by

$$d\sigma = \frac{1}{(2\pi)^5} \frac{M_d M_\Sigma M_n}{4k_{c.m.} E_{c.m.}^2} |\mathcal{T}|^2 |\vec{p}_\pi^*| |\vec{p}_n| dM_{\pi\Sigma} d\Omega_\pi^* d\Omega_n \quad (1)$$

where \mathcal{T} is the T -matrix of this reaction, $E_{c.m.}$ is the center of mass energy, $k_{c.m.}$ is the kaon c.m. momentum and \vec{p}_π^* is the pion momentum in the rest frame of π and Σ . The pion momentum $|\vec{p}_\pi^*|$ in the $\pi\Sigma$ rest frame can be fixed by the invariant mass $M_{\pi\Sigma}$ as

$$|\vec{p}_\pi^*| = \frac{\lambda^{1/2}(M_{\pi\Sigma}^2, m_\pi^2, M_\Sigma^2)}{2M_{\pi\Sigma}} \quad (2)$$

with the Källén function $\lambda(x, y, z) = x^2 + y^2 + z^2 - 2xy - 2yz - 2zx$.

The $\Lambda(1405)$ production is investigated by limiting the kinematics with the invariant mass of the final $\pi\Sigma$ state around 1350 to 1450 MeV, in which the resonating $\pi\Sigma$ forms the $\Lambda(1405)$ and the resonance contribution may dominate the cross section. Thus, we do not consider the diagrams in which the final π and Σ are emitted from different vertices, since they are not correlated. In this $\Lambda(1405)$ dominance approximation, we have three diagrams for this reaction as shown in Fig. 2. The left diagram of Fig. 2 expresses the $\Lambda(1405)$ production in the impulse approximation. We refer to this diagram as direct production process. The middle and right diagrams are for two-step processes with \bar{K} exchange. We refer to these diagrams as double scattering diagrams.

In Fig. 2, T_1 and T_2 denote s -wave scattering amplitudes of $\bar{K}N \rightarrow \bar{K}N$ and $\bar{K}N \rightarrow \pi\Sigma$, respectively. These amplitudes are calculated in coupled-channels approach based on chiral dynamics, as we will explain later. In the amplitude T_2 , the $\Lambda(1405)$ resonance is involved. Note that, in these three diagrams, the $\Lambda(1405)$ in the amplitude T_2 is produced by the $\bar{K}N$ channel. For the amplitude T_1 , the energies of interest are 1600 MeV to 1800 MeV for the K^- incident momenta 600 MeV/c to 1000 MeV/c in the lab. frame. We do not consider the diagrams where π and Σ come from different vertices, for example, a double scattering diagram with pion exchange, in which Σ and π are emitted from the T_1 and T_2 amplitudes, respectively. Such diagrams may give smooth backgrounds in the $\pi\Sigma$ invariant mass spectra. We do not consider the $\Sigma(1385)$ resonance in the T_2 amplitude, since the branching rate of $\Sigma(1385)$ to $\pi\Sigma$ is only 12%.

B. Scattering amplitude

Let us calculate the T -matrix for the $K^-d \rightarrow \pi\Sigma n$ reaction. The T -matrix for the diagram 1 given in Fig. 2 can be calculated in the impulse approximation in which the incident K^- and the proton in the deuteron transform into $\pi\Sigma$ and the neutron behaves as a spectator of the reaction.

Letting the wavefunctions of the incident kaon and the particles in the final state be given by plane waves and writing the wavefunctions of the nucleons in the deuteron as φ_i ($i = 1, 2$), we obtain the connected part of the S -matrix:

$$S = \int d^4x_1 (-i) T_{K^-p \rightarrow \pi\Sigma} \mathcal{N}_\Sigma e^{ip_\Sigma \cdot x_1} \mathcal{N}_\pi e^{ip_\pi \cdot x_1} \times \mathcal{N}_1 \varphi_1(\vec{x}_1) e^{-ip_1^0 x_1^0} \mathcal{N}_{K^-} e^{-ik \cdot x_1} \times \int d^3x_2 \mathcal{N}_n e^{-i\vec{p}_n \cdot \vec{x}_2} \mathcal{N}_2 \varphi_2(\vec{x}_2) \quad (3)$$

where $T_{K^-p \rightarrow \pi\Sigma}$ is the T -matrix for the $K^-p \rightarrow \pi\Sigma$, and p_1 and p_2 are the momenta of the proton and neutron inside the deuteron, respectively. The normalization factors of the wavefunctions are given by $\mathcal{N}_i = \sqrt{M_i/E_i}$ for baryons and $\mathcal{N}_a = 1/\sqrt{2\omega_a}$ for mesons. The plane waves are normalized inside a box with a unit volume.

The integration of the time component x_1^0 give the delta function for energy conservation:

$$\int dx_1^0 e^{-i(k^0 + p_1^0 - p_\Sigma^0 - p_\pi^0)x_1^0} = 2\pi \delta(k^0 + p_1^0 - p_\Sigma^0 - p_\pi^0). \quad (4)$$

In the impulse approximation, the energy of the spectator neutron does not change, $p_2^0 = p_n^0$. Taking the deuteron energy as the sum of the energies of the nucleons, $p_d^0 = p_1^0 + p_2^0$, we obtain the total energy conservation $k^0 + p_d^0 - p_\Sigma^0 - p_\pi^0 - p_n^0 = 0$. Here, in general, $p_n^0 \neq p_2^0$. Thus one must assume in the impulse approximation that the initial energy in the deuteron is not equally distributed between the two nucleons.

To perform the spacial integrals, we introduce the relative coordinate for \vec{x}_1 and \vec{x}_2 as $\vec{R} = (\vec{x}_1 + \vec{x}_2)/2$ and $\vec{r} = \vec{x}_1 - \vec{x}_2$. We also introduce the deuteron wavefunction for the relative motion $\varphi(r)$ and assume that the center of mass motion of the deuteron is described as the plane wave. Namely we replace the nucleon wavefunctions, $\varphi_1(\vec{x}_1)$ and $\varphi_2(\vec{x}_2)$, as follows:

$$\mathcal{N}_1 \mathcal{N}_2 \varphi_1(\vec{x}_1) \varphi_2(\vec{x}_2) \rightarrow \mathcal{N}_d e^{i\vec{p}_d \cdot \vec{R}} \varphi(\vec{r}) \quad (5)$$

where the deuteron wavefunction is normalized as

$$\int d^3r |\varphi(\vec{r})|^2 = 1. \quad (6)$$

We neglect d -wave component of the deuteron wavefunction. The s -wave wavefunction $\varphi(r)$ is parametrized by analytic functions [15] as

$$\varphi(r) = \sum_{j=1}^{11} C_j \exp(-m_j r). \quad (7)$$

We use the parametrization for C_j and m_j given in Ref. [16]. The integration in terms of \vec{R} gives the delta function for total momentum conservation, while the integration of \vec{r} gives the Fourier transformation of the deuteron wavefunction:

$$\int d^3r \varphi(r) e^{i(\vec{k} + \vec{p}_n - \vec{p}_\Sigma - \vec{p}_\pi) \cdot \frac{\vec{r}}{2}} = \tilde{\varphi}(\vec{p}_n - \frac{\vec{p}_d}{2}) \quad (8)$$

where we have used momentum conservation.

Finally we obtain the S -matrix for the diagram 1 as

$$S = -iT_{K^-p \rightarrow \pi\Sigma} \varphi(\vec{p}_n - \frac{\vec{p}_d}{2}) \mathcal{N}_d \mathcal{N}_K \mathcal{N}_\Sigma \mathcal{N}_\pi \mathcal{N}_n \times (2\pi)^4 \delta^4(p_d + k - p_\Sigma - p_\pi - p_n). \quad (9)$$

Since the T -matrix is given by $S = 1 - i(2\pi)^4 \delta^4(p_d + k - p_\Sigma - p_\pi - p_n) (\prod_i \mathcal{N}_i) \mathcal{T}$, we obtain the T -matrix for the diagram 1 as

$$\mathcal{T}_1 = T_{K^-p \rightarrow \pi\Sigma}(M_{\pi\Sigma}) \varphi(\vec{p}_n - \frac{\vec{p}_d}{2}). \quad (10)$$

Next let us consider the double scattering diagrams shown as diagrams 2 and 3 in Fig. 2. In the same way as the calculation of diagram 1, the connected S -matrix for diagram 2 is obtained as

$$S = \left(\prod_i \mathcal{N}_i \right) \int d^4x_1 \int d^4x_2 (i) \int \frac{d^4q}{(2\pi)^4} \frac{e^{-iq \cdot (x_1 - x_2)}}{q^2 - m_K^2 + i\epsilon} \times e^{ip_\Sigma \cdot x_1} e^{ip_\pi \cdot x_1} e^{ip_n \cdot x_2} e^{-ik \cdot x_2} e^{-ip_1^0 x_1^0} \varphi_1(\vec{x}_1) \times e^{-ip_2^0 x_2^0} \varphi_2(\vec{x}_2) (-i) T_{K^-n \rightarrow K^-n} (-i) T_{K^-p \rightarrow \pi\Sigma}. \quad (11)$$

The integrations with respect to x_1^0 and x_2^0 give energy conservation $p_1^0 + q^0 = p_\Sigma^0 + p_\pi^0$ and $p_2^0 + k^0 = q^0 + p_n^0$, respectively. Integrating with respect to q_0

$$\int \frac{dq_0}{2\pi} 2\pi \delta(p_1^0 + q^0 - p_\Sigma^0 - p_\pi^0) 2\pi \delta(p_2^0 + k^0 - q^0 - p_n^0) = 2\pi \delta(k^0 + p_d^0 - p_\Sigma^0 - p_\pi^0 - p_n^0) \quad (12)$$

we obtain total energy conservation and q^0 has been fixed as $q^0 = k^0 + p_2^0 - p_n^0 = p_\Sigma^0 + p_\pi^0 - p_1^0$. Here we have used again $p_1^0 + p_2^0 = p_d^0$. Introducing again the relative coordinate for \vec{x}_1 and \vec{x}_2 and the deuteron wavefunction as Eq. (5), we find that the integration with respect to \vec{R} gives total momentum conservation and that the integration of \vec{r} provides the Fourier transformation of the deuteron wavefunction:

$$\int d^3r \varphi(r) e^{i(-\vec{k} + \vec{p}_n - \vec{p}_\Sigma - \vec{p}_\pi + 2\vec{q}) \cdot \frac{\vec{r}}{2}} = \tilde{\varphi}(\vec{q} + \vec{p}_n - \vec{k} - \frac{\vec{p}_d}{2})$$

with momentum conservation $\vec{p}_\Sigma + \vec{p}_\pi = \vec{p}_d + \vec{k} - \vec{p}_n$. Finally we obtain the T -matrix for diagram 2 as

$$\mathcal{T}_2 = T_{K^-n \rightarrow K^-n}(W) T_{K^-p \rightarrow \pi\Sigma}(M_{\pi\Sigma}) \times \int \frac{d^3q}{(2\pi)^3} \frac{\tilde{\varphi}(\vec{q} + \vec{p}_n - \vec{k} - \frac{\vec{p}_d}{2})}{q^2 - m_K^2 + i\epsilon}. \quad (13)$$

where W denotes the invariant mass of the initial kaon and the neutron inside the deuteron, $W \equiv \sqrt{(k + p_2)^2}$.

The variables W and q^0 are fixed by kinematics but depend on energies of the nucleons in the deuteron. To evaluate these values, let us take the deuteron rest frame, that is, the laboratory frame. The deuteron is a loosely bound system of proton and neutron with about 2 MeV binding energy. Neglecting the binding energy for the neutron, we evaluate

$$q^0 = M_N + k^0 - p_n^0. \quad (14)$$

The wavefunction of the nucleons inside the deuteron in momentum space has the largest component when the nucleon is almost at rest in the rest frame of the deuteron. This fact allows us to determine W as

$$W \equiv \sqrt{(k + p_2)^2} \cong \sqrt{(M_N + k^0)^2 - \vec{k}^2}. \quad (15)$$

Note that, under this assumption, the energy W for the $K^-n \rightarrow K^-n$ amplitude is completely fixed by kinematics without depending on the momenta of the final state. Thus, the value of the $K^-n \rightarrow K^-n$ scattering amplitude contributes only to the absolute value of the cross section and does not provide any structure in the invariant mass spectra.

In the same way, we can calculate the T -matrix for diagram 3:

$$\mathcal{T}_3 = -T_{K^-p \rightarrow \bar{K}^0 n}(W) T_{\bar{K}^0 n \rightarrow \pi\Sigma}(M_{\pi\Sigma}) \times \int \frac{d^3q}{(2\pi)^3} \frac{\tilde{\varphi}(\vec{q} + \vec{p}_n - \vec{k} - \frac{\vec{p}_d}{2})}{q^2 - m_K^2 + i\epsilon}. \quad (16)$$

The negative sign in the right had side comes from the isospin configuration of the deuteron.

Finally, the total T -matrix is given by summing up these three amplitudes:

$$\mathcal{T} = \mathcal{T}_1 + \mathcal{T}_2 + \mathcal{T}_3 \quad (17)$$

where \mathcal{T}_i ($i = 1, 2, 3$) are given in Eqs. (10), (13) and (16), respectively. Note again that, in these amplitudes \mathcal{T}_i ($i = 1, 2, 3$), the $\Lambda(1405)$ is involved in the $\bar{K}N$ -initiated amplitudes $T_{\bar{K}N \rightarrow \pi\Sigma}$.

C. Description of the $\bar{K}N$ scattering amplitudes and model for the $\Lambda(1405)$

For the description of the $\Lambda(1405)$, we use the chiral unitary approach, in which the $\Lambda(1405)$ is dynamically generated in coupled-channels of meson-baryon scattering with strangeness $S = -1$ and charge $Q = 0$, namely K^-p , \bar{K}^0n , $\pi^0\Lambda$, $\pi^0\Sigma^0$, $\eta\Lambda$, $\eta\Sigma^0$, $\pi^+\Sigma^-$, $\pi^-\Sigma^+$, $K^+\Xi^-$ and $K^0\Xi^0$. The scattering amplitudes for the meson-baryon channels are obtained by solving the Bethe-Salpeter equation with the s -wave interaction kernels V given by chiral Lagrangian. The Bethe-Salpeter equation turns out to be an algebraic equation of the meson-baryon coupled channels if we consider elastic unitarity in the N/D method [4]:

$$T_{ij}(W) = V_{ij}(W) + V_{ik}(W)G_k(W)T_{kj}(W). \quad (18)$$

where i, j are the channel indices given in Ref. [3] and W denotes the center of mass energy.

In Eq. (18), V is given by the leading order of the chiral Lagrangian as

$$V_{ij}(W) = -\frac{C_{ij}}{4f^2}(2W - M_i - M_j) \left(\frac{M_i + E_i}{2M_i}\right)^{1/2} \left(\frac{M_j + E_j}{2M_j}\right)^{1/2} \quad (19)$$

with the baryon masses M_i and energy E_i . The coefficient C_{ij} in Eq. (19) is the channel coupling which is fixed by the flavor SU(3) group structure, and f is the decay constant of the meson in the chiral field $U = \exp[i\sqrt{2}\Phi/f]$. Here we take $f = 1.123f_\pi$ with $f_\pi = 93$ MeV [5].

The diagonal matrix $G_k(W)$ in Eq. (18) is a meson-baryon loop function and is evaluated with dimensional regularization:

$$\begin{aligned} G_k(W) &= i \int \frac{d^4q}{(2\pi)^4} \frac{2M_k}{(P-q)^2 - M_k^2 + i\epsilon} \frac{1}{q^2 - m_k^2 + i\epsilon} \\ &= \frac{2M_k}{16\pi^2} \left\{ a_k(\mu) + \ln \frac{M_k}{\mu^2} + \frac{m_k^2 - M_k^2 + W^2}{2W^2} \ln \frac{m_k^2}{M_k^2} \right. \\ &\quad + \frac{\bar{q}_k}{W} [\ln(W^2 - (M_k^2 - m_k^2) + 2\bar{q}_k W) \\ &\quad + \ln(W^2 + (M_k^2 - m_k^2) + 2\bar{q}_k W) \\ &\quad - \ln(-W^2 + (M_k^2 - m_k^2) + 2\bar{q}_k W) \\ &\quad \left. - \ln(-W^2 - (M_k^2 - m_k^2) + 2\bar{q}_k W) \right\} \quad (20) \end{aligned}$$

where m_i is the meson mass, \bar{q}_i is the center of mass momentum and $a_i(\mu)$ is the subtraction constant with a renormalization scale μ . The subtraction constants are only the free parameters in this model and are determined so as to reproduce the threshold properties of K^-p to several channels [2], which were obtained by K^- absorptions of Kaonic hydrogen [17]. In a recent work [8], it is found that the values of the subtraction constant are very important to determine the nature of the dynamically generated resonances in the chiral unitary approach.

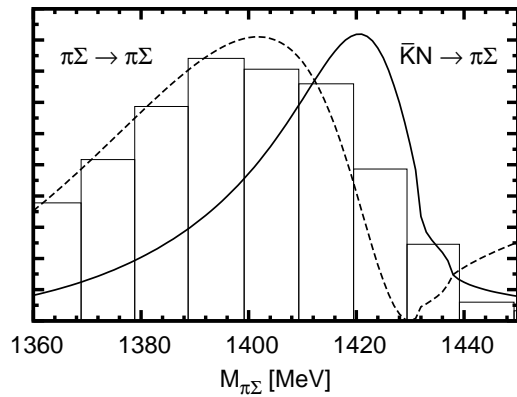


FIG. 3: $\pi\Sigma$ invariant mass spectra of two-body scatterings of $\bar{K}N \rightarrow \pi\Sigma$ (solid line) and $\pi\Sigma \rightarrow \pi\Sigma$ (dashed line) with $I = 0$ in arbitrary units. The histogram denotes an experimental data in Ref. [18].

Here we take a standard parameter set given in Ref. [5]:

$$\begin{aligned} a_{\bar{K}N} &= -1.84, & a_{\pi\Sigma} &= -2.00, & a_{\pi\Lambda} &= -1.83, \\ a_{\eta\Lambda} &= -2.25, & a_{\eta\Sigma} &= -2.38, & a_{K\Xi} &= -2.67, \end{aligned} \quad (21)$$

with $\mu = 630$ MeV. The scattering amplitudes calculated with this parameter set reproduce well the $\pi\Sigma$ invariant mass spectrum and the total cross sections of K^-p to several channels [5], and the $\Lambda(1405)$ is found to be almost a purely dynamical state of meson and baryon [8].

We use the scattering amplitudes obtained in the chiral unitary approach described above for the $\bar{K}N \rightarrow \bar{K}N$ and $\bar{K}N \rightarrow \pi\Sigma$ amplitudes in Eqs. (10), (13) and (16). After fixing the subtraction parameters $a_i(\mu)$ in the two-body scattering, we have no adjustable parameters for the calculation of the $K^-p \rightarrow \pi\Sigma n$ reaction in the present approach.

The scattering amplitudes obtained in the chiral unitary approach have notable features. The $\Lambda(1405)$ is successfully reproduced by meson-baryon dynamics, but the resonance position depends on the channels [9]. In Fig. 3, we plot the $\pi\Sigma$ invariant mass distributions for $\bar{K}N \rightarrow \pi\Sigma$ and $\pi\Sigma \rightarrow \pi\Sigma$ with $I = 0$ defined by

$$\frac{d\sigma_{MB}}{dM_{\pi\Sigma}} = A|T|^2 q_{c.m.} \quad (22)$$

where A is a constant, $q_{c.m.}$ is the CM momentum of the final $\pi\Sigma$ state and T is the two-body meson-baryon scattering amplitude. We also show in Fig. 3, as the histogram, the experimental data of the $\pi^-\Sigma^+$ invariant mass spectrum obtained in $K^-p \rightarrow \Sigma^+\pi^-\pi^+\pi^-$ at 4.2 GeV/c for a K^- beam with the restriction of the $\Sigma^+\pi^-\pi^+$ invariant mass being between 1.6 to 1.72 GeV at which the $\Sigma(1660)$ resonance (acting as a doorway of the reaction) is located [18].

As seen in Fig. 3, the line shapes of these two channels are significantly different and the peak position in the $\pi\Sigma$ initiated scattering is 20 MeV lower than in $\bar{K}N$

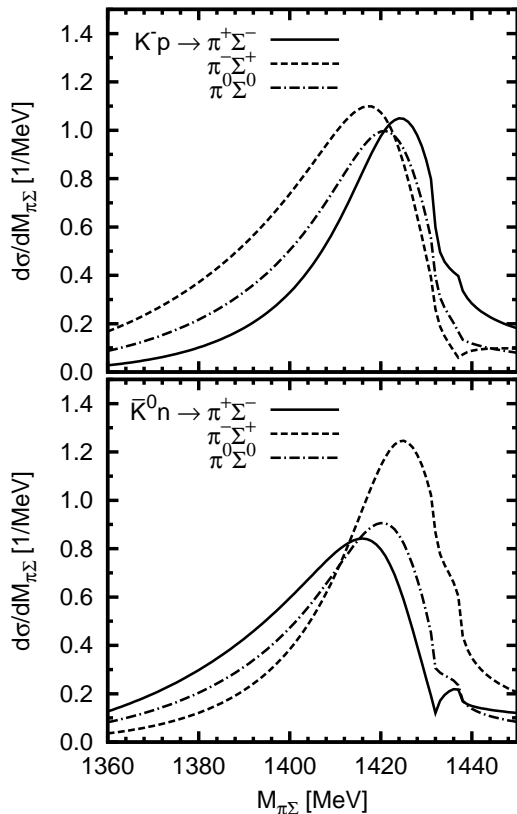


FIG. 4: $\pi\Sigma$ invariant mass spectra of two-body scatterings of $K^-p \rightarrow \pi\Sigma$ (upper panel) and $\bar{K}^0n \rightarrow \pi\Sigma$ (lower panel) for different $\pi\Sigma$ charged states. We take $A = 1$ in Eq. (22).

scattering. This is because $\pi\Sigma$ is so strongly correlated as to produce the lower mass resonance pole in these energies¹. As already discussed above, in the present process $K^-d \rightarrow \Lambda(1405)n$, the $\Lambda(1405)$ is driven by the $\bar{K}N$ channel. Thus, it is expected that the $\Lambda(1405)$ spectrum shape has a peak around 1420 MeV instead of 1405 MeV.

We also remark that the $\Lambda(1405)$ line shapes are moderately different in different charged states of the π and Σ . This is simply due to the interference of $I = 0$ and $I = 1$ components in the scattering amplitudes [19]. For later convenience we show the mass spectra (22) for K^-p and \bar{K}^0n to $\pi^\pm\Sigma^\mp$ and $\pi^0\Sigma^0$ in Fig. 4.

For the amplitude T_1 in Fig. 2, we plot, in Fig. 5, the modules of the $\bar{K}N$ scattering amplitudes in the relevant energy region to the present calculation. The $K^-n \rightarrow K^-n$ amplitude appearing in diagram 2 is about a factor 3 larger than $K^-p \rightarrow \bar{K}^0n$ in diagram 3 for the energy range from $E_{c.m.} = 1600$ to 1800 MeV. Thus, we expect that diagram 2 gives a larger contribution than diagram 3 for the incident K^- momenta from 600 to 1000 MeV/c.

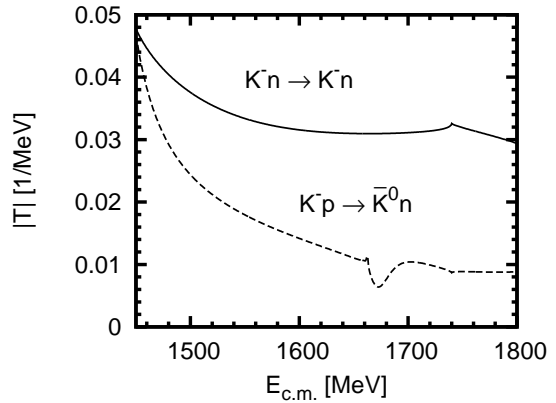


FIG. 5: Modules of $\bar{K}N$ scattering amplitude obtained in the chiral unitary approach.

The dip structure around 1670 MeV in $K^-p \rightarrow \bar{K}^0n$ is due to the presence of the $\Lambda(1670)$ resonance with $I = 0$, while $K^-n \rightarrow K^-n$ has purely $I = 1$ and there is no structure for the $\Lambda(1670)$.

III. RESULTS

In this section, we show the numerical results of the calculations for the $K^-d \rightarrow \pi\Sigma n$ reaction. The $\pi\Sigma$ invariant mass is calculated by

$$\frac{d\sigma}{dM_{\pi\Sigma}} = \frac{M_d M_\Sigma M_n}{(2\pi)^5 4k_{c.m.} E_{c.m.}^2} \int |\mathcal{T}|^2 |\vec{p}_\pi^*| |\vec{p}_n| d\Omega_\pi^* d\Omega_n \quad (23)$$

where $(|\vec{p}_\pi^*|, \Omega_\pi^*)$ is the π momentum in the rest frame of the $\pi\Sigma$ state. The T -matrix \mathcal{T} is evaluated as a sum of the amplitudes given in Eqs. (10), (13) and (16). These amplitudes contain two-body meson-baryon scattering amplitudes of $\bar{K}N \rightarrow \bar{K}N$ and $\bar{K}N \rightarrow \pi\Sigma$. These amplitudes are calculated in the chiral unitary approach described in Sec. II C. The $\bar{K}N \rightarrow \bar{K}N$ scattering amplitudes are functions of the c.m. energy of the incident kaon and one of the nucleons in the deuteron, which can be determined when the initial kaon momentum is fixed, as discussed in Eq. (15), while the $\bar{K}N \rightarrow \pi\Sigma$ amplitudes are functions of the $\pi\Sigma$ invariant mass $M_{\pi\Sigma}$ and provide the resonance shape for the $\Lambda(1405)$.

A. Comparison with the experimental data of $K^-d \rightarrow \pi^+\Sigma^-n$

First of all, we compare our theoretical calculation of the $K^-d \rightarrow \pi^+\Sigma^-n$ reaction with the experimental data reported in Ref. [21]. The experiment was performed with K^- having momenta between 686 and 844 MeV/c and the particles were detected by bubble chamber.

¹ The importance of the strong $\pi\Sigma$ correlation in $\bar{K}N$ subthreshold scattering with $S = -1$ was recently pointed out in Ref. [20].

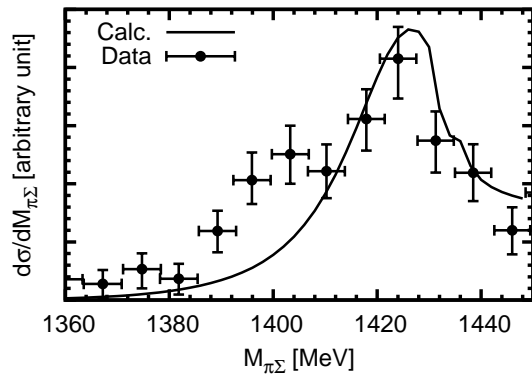


FIG. 6: $\pi\Sigma$ invariant mass spectra of $K^-d \rightarrow \pi^+\Sigma^-n$ in arbitrary units at 800 MeV/c incident K^- momentum. The solid line denotes the present calculation. The data are taken from the bubble chamber experiment at K^- momenta between 686 and 844 MeV/c given in Ref. [21].

1. $\pi^+\Sigma^-$ invariant mass spectrum

We show, in Fig. 6, the $\pi^+\Sigma^-$ invariant-mass spectrum in arbitrary units at 800 MeV/c incident K^- momentum and compare our theoretical calculation with the experimental data. The data are taken from the bubble chamber experiment at K^- momenta between 686 and 844 MeV/c [21]. In the analysis of this experiment, the resonance contribution was determined by fitting a relativistic Breit-Wigner distributions and a smooth background parametrized as a sum of Legendre polynomials to the data. We show, in Fig. 6, the resonance (foreground) contributions for the experimental data which are obtained by subtracting the background contributions estimated with the Legendre polynomials in Ref. [21] from the actual data points given in the paper. The solid line denotes our theoretical calculation with the chiral unitary approach.

The spectrum shape obtained in this calculation agrees with that of the experimental observation. Especially it is very interesting to see that the peak position, which comes from the $\Lambda(1405)$ production, appears around $M_{\pi\Sigma} = 1420$ MeV instead of 1405 MeV announced nominally by the Particle Data Group. This is one of the strongest evidences that the resonance position of the $\Lambda(1405)$ depends on the initial channel of meson and baryon, and supports the double pole nature of the $\Lambda(1405)$, in which the higher state sitting in 1420 MeV strongly couples to the $\bar{K}N$ channel. The bump structure seen around $M_{\pi\Sigma} = 1390$ MeV is probably related to the p -wave contributions coming from the $\Sigma^*(1385)$ production, which did not take into account in the present calculation.

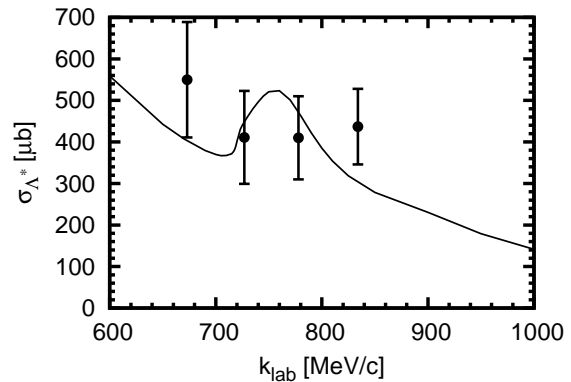


FIG. 7: Incident K^- momentum dependence of the $\Lambda(1405)$ production cross section calculated with the $K^-d \rightarrow \pi^+\Sigma^-n$ reaction. The data are taken from Ref. [21].

2. Λ^* production cross section

We also estimate the production cross section of the $\Lambda(1405)$ in the $K^-d \rightarrow \Lambda(1405)n$ reaction by integrating the spectrum obtained in our calculation over the $\pi\Sigma$ invariant mass around the resonance peak:

$$\sigma_{\Lambda^*} = 3 \int_{M_{\min}}^{M_{\max}} dM_{\pi^+\Sigma^-} \frac{d\sigma}{dM_{\pi^+\Sigma^-}}. \quad (24)$$

The factor 3 accounts for the branching ratio of $\Lambda(1405) \rightarrow \pi^+\Sigma^-$. Taking $M_{\min} = 1400$ MeV and $M_{\max} = 1440$ MeV read from the figure, we obtain the $\Lambda(1405)$ production cross section as $385 \mu\text{b}$ with 800 MeV/c incident K^- . An experimental value observed in the $K^-d \rightarrow \pi^+\Sigma^-n$ reaction is reported to be $410 \pm 100 \mu\text{b}$ at 778 MeV/c of the incident K^- momentum [21]. The present calculation fairly agrees with the observed value. This implies that the $\Lambda(1405)$ production mechanism in the present reaction is explained by the three diagrams shown in Fig. 2.

In Fig. 7, we show the incident momentum dependence of the $\Lambda(1405)$ production cross section. The cross sections are evaluated from the $K^-d \rightarrow \pi^+\Sigma^-n$ channel by integrating the invariant mass spectra from 1400 MeV to 1440 MeV and multiplying by the isospin factor 3. The experimental data are taken again from Ref. [21]. Our calculation is consistent with the experimental data. The bump structure seen in the theoretical calculation around $k_{\text{lab}} = 750$ MeV/c corresponds to the $\Lambda(1670)$ resonance production in the T_1 amplitude of $K^-p \rightarrow \bar{K}^0n$ (see Fig. 2).

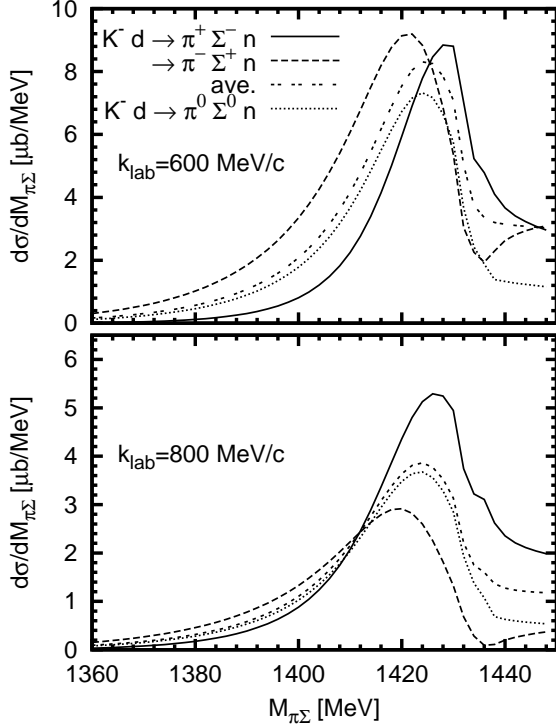


FIG. 8: $\pi\Sigma$ invariant mass spectra of $K^-d \rightarrow \pi\Sigma n$ with different charged $\pi\Sigma$ states. The solid, dashed and dotted lines denote the invariant mass spectra of $\pi^+\Sigma^-$, $\pi^-\Sigma^+$ and $\pi^0\Sigma^0$ for the final $\pi\Sigma$ state, respectively. The double-dotted line shows the averaged spectrum of $\pi^+\Sigma^-$ and $\pi^-\Sigma^+$ of the final $\pi\Sigma$ states.

B. Theoretical results of the $\pi\Sigma$ invariant mass spectra

1. Spectra of other $\pi\Sigma$ charged states

In the previous section, we have seen that the $\Lambda(1405)$ resonance appears around 1420 MeV in the $\pi^+\Sigma^-$ invariant mass spectrum. To confirm that the resonance position of the $\Lambda(1405)$ in the \bar{K} induced processes is higher than the nominal $\Lambda(1405)$, it is certainly necessary to project out the $I = 0$ contributions from the invariant mass spectra, since the shift of the resonance position could be explained by interference between the $I = 0$ $\Lambda(1405)$ resonance and non-resonant $I = 1$ $\pi\Sigma$ correlations.

In Fig. 8, we plot the $\pi\Sigma$ invariant mass spectra for the different charged $\pi\Sigma$ states with incident K^- momenta of 600 and 800 MeV/c. We also plot the averaged spectrum of $K^-d \rightarrow \pi^+\Sigma^-n$ and $K^-d \rightarrow \pi^-\Sigma^+n$, in which interference terms of $I = 0$ and $I = 1$ in the $\pi\Sigma$ correlation are cancelled out. In the spectrum of $K^-d \rightarrow \pi^0\Sigma^0n$, there are not $I = 1$ contributions in the $\pi\Sigma$ system.

The peak positions are slightly dependent on the charged channels due to the interference between the $\Lambda(1405)$ resonance with $I = 0$ and non-resonant $\pi\Sigma$ scat-

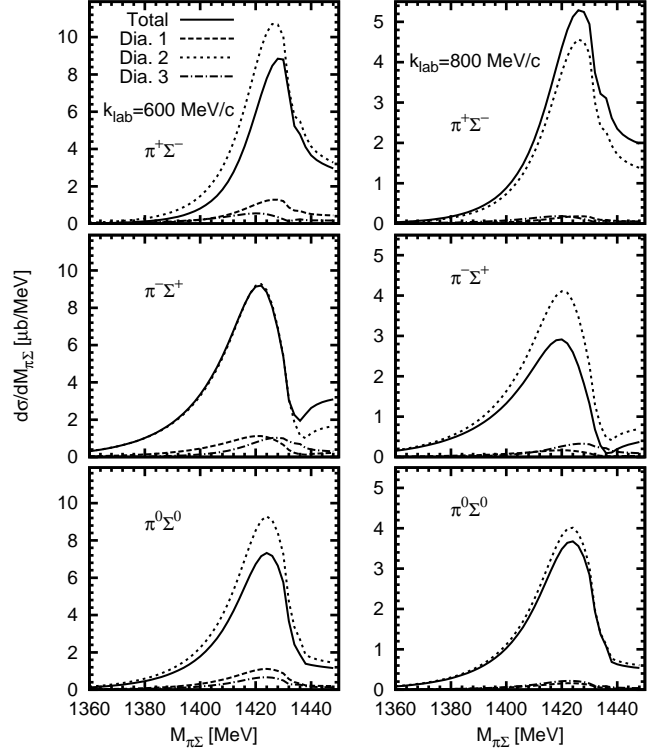


FIG. 9: $\pi\Sigma$ invariant mass spectra of $K^-d \rightarrow \pi\Sigma n$ separately plotted in each diagram contribution. The solid line denotes the total contributions of three diagrams. The dashed, dotted and dash-dotted lines show the calculations from diagram 1, 2 and 3 shown in Fig. 2, respectively. The plots in the left and right panels are calculated with 600 and 800 MeV/c of K^- incident momenta, respectively. The charge states of $\pi\Sigma$ are shown in the plots.

tering with $I = 1$. The differences are within several MeV. The peak positions are insensitive to the incident K^- momenta, but the heights are dependent on the K^- momenta. This is because the contribution from each diagram depends on the incident momentum and interference between the diagrams shown in Fig. 2 makes the heights of the spectrum dependent on the incident momentum.

2. Contributions from each diagram

In Fig. 9 we show the $\pi\Sigma$ invariant mass spectra with separated contributions from the diagrams shown in Fig. 2. In the diagram 1, the $\Lambda(1405)$ resonance is created by the incident K^- and the proton inside the deuteron, and the neutron is a spectator of the $\Lambda(1405)$ production. In the diagrams 2 and 3, two nucleons contribute the $\Lambda(1405)$ production with one kaon exchange. In Fig. 9, we find that the diagram 2 gives the dominant contribution to the total spectrum and that the impulse approximation diagram 1 is negligible, specially at higher

incident momenta. The reason why the two-nucleon processes give large contributions can be understood as follows. In the present reaction the $\Lambda(1405)$ is produced by the $\bar{K}N$ channel below its threshold. Thus, some amount of energy should be taken out by the final neutron with energy transfer between the nucleons. In the double scattering processes (diagrams 2 and 3), the transferred energy is taken from the initial kaon, such that the exchanged kaon carries less energy than on shell. In the impulse process of the diagram 1, the energy should be transferred by the relative motion of the nucleons inside the deuteron. Due to the small binding energy of the deuteron, the deuteron wavefunction has small high energy components. Therefore, the contribution of the diagram 1 is negligibly small. The reason that the diagram 3 is relatively smaller than diagram 2 is that the s -wave $K^-p \rightarrow \bar{K}^0n$ amplitude in the diagram 3 is smaller than the $K^-n \rightarrow K^-n$ in the diagram 2 at the present energy region as seen in Fig. 5.

3. Angular dependence of the $\Lambda(1405)$ production cross section

In Fig. 10, we plot the angular dependence of the $\Lambda(1405)$ production cross section of a function of the angle of the incident kaon and the outgoing neutron in the center of mass frame. The differential cross section is calculated by

$$\frac{d\sigma_{\Lambda^*}}{d\cos\theta} = \int_{M_{\min}}^{M_{\max}} dM_{\pi\Sigma} \frac{d\sigma}{dM_{\pi\Sigma}d\cos\theta} \quad (25)$$

with $M_{\min} = 1400$ MeV and $M_{\max} = 1440$ MeV. Here we do not multiply by a factor 3, since we consider the production cross section of each final $\pi\Sigma$ state.

There are two contributions for the $\Lambda(1405)$ production. One is backward Λ^* production ($\theta_{\text{c.m.}}^n \simeq 0^\circ$) and the other one is forward production ($\theta_{\text{c.m.}}^n \simeq 180^\circ$). Figure 10 shows that large contributions to the total $\Lambda(1405)$ production come from the backward production.

The forward Λ^* production with $\theta_{\text{c.m.}}^n > 150^\circ$ comes from diagram 1 in Fig. 2. As already mentioned, in this diagram the neutron inside the deuteron can be regarded as a spectator of the $\Lambda(1405)$ production from K^-p . Therefore the neutron goes to the backward angles $\theta_{\text{c.m.}}^n > 150^\circ$. On the other hand, in the double scattering processes (diagram 2 and 3), the energetic incident kaon kicks one of the nucleons in the deuteron to forward directions and the exchanged kaon goes to backward angles. The recoil momentum depends on the emitted nucleon angles and gets smaller with larger recoil angles. The exchanged kaon going backward produces the $\Lambda(1405)$ together with the other nucleon in the deuteron. Since the momentum distribution of the nucleons in the deuteron is concentrated at low momenta, less than 100 MeV/c, a good momentum matching to create the $\Lambda(1405)$ is achieved by small momenta of the exchanged kaon, namely large momentum transfer of the

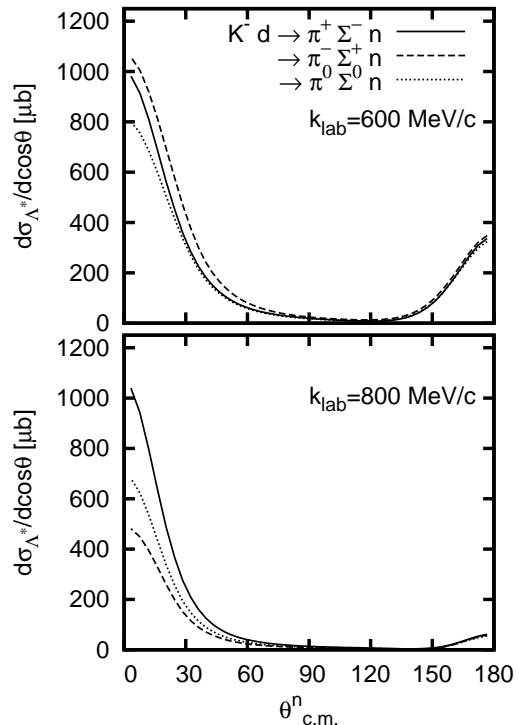


FIG. 10: Angular dependence of the $\Lambda(1405)$ production cross section. The horizontal axis is the angle between the incident kaon and the emitted neutron in center of mass frame. The incident K^- momenta are 600 MeV/c and 800 MeV/c in the upper and lower panels, respectively.

incident K^- to the emitted neutron. Therefore, in the double scattering processes, the production rate of the $\Lambda(1405)$ is dominated by the backward angles.

4. Incident K^- momentum dependence

As we have already shown in Fig. 7, the $\Lambda(1405)$ production cross section in $K^-d \rightarrow \pi^+\Sigma^-n$ decreases as the incident K^- momentum increases. This is because more energetic incident K^- produce the $\Lambda(1405)$ less efficiently due to worse momentum matching between the kaons and the nucleons inside the deuteron in both direct production (diagram 1) and double scattering (diagram 2 and 3) processes.

In Fig. 11, we show the incident momentum dependence of the $\pi\Sigma$ invariant spectra of the $K^-d \rightarrow \pi^+\Sigma^-n$ reaction. We find that the height of the resonance peak for the $\Lambda(1405)$ around 1420 MeV has a strong incident momentum dependence, as seen in the production cross section, but the spectrum shapes do not depend on the incident energy.

For lower momenta of the incident K^- , since the production cross sections of the $\Lambda(1405)$ are enhanced, one would expect some advantage to observe the $\Lambda(1405)$ using low energy incident K^- . This is true for not very

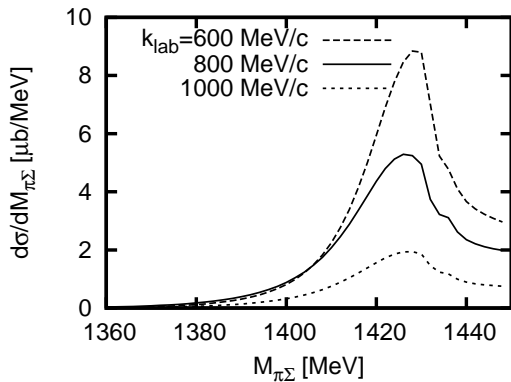


FIG. 11: $\pi\Sigma$ invariant mass spectra of the $K^-d \rightarrow \pi^+\Sigma^-n$ reaction with 600, 800 and 1000 MeV/c incident K^- momenta.

low momenta of the incident K^- . For instance, we plot the $\pi\Sigma$ invariant mass spectra at 400 MeV/c incident K^- momentum in the right panel of Fig. 12. These figures show that the heights of the spectra are about five times larger than those of the spectra obtained with 600 MeV/c of the incident K^- , and that the spectrum shapes are very similar to each other. Thus, using 400 MeV/c incident K^- is better to observe the $\Lambda(1405)$ spectra. It is also seen that diagram 1 and 3 give a moderate contribution to the spectra, as seen in Fig. 12. We show also the angular dependence of the $\Lambda(1405)$ production cross sections in Fig. 13. Due to the substantial contribution from diagram 1, which is the single step process, the $\Lambda(1405)$ is produced also at forward angles.

For further low incident momenta, the spectra can be distorted by threshold effects. We show the $\pi\Sigma$ invariant mass spectra for the 200 MeV/c incident K^- in the left panel of Fig. 12. As seen in Fig. 12 for the $\pi^+\Sigma^-$ spectrum, the signal of the $\Lambda(1405)$ production is distorted by the strong contributions around 1440 MeV. The maximum invariant mass $M_{\pi\Sigma}$ is at 1460 MeV for the 200 MeV/c incident K^- . Since the $\Lambda(1405)$ is produced in the s -wave of $\pi\Sigma$, the phase space suppression around the threshold shows up only at invariant masses very close to the maximum of the invariant mass. For the incident momentum of 200 MeV/c, diagram 1 gives the dominant contributions, as seen in Fig. 12. This has as a consequence that most of the $\Lambda(1405)$ is produced at forward angles (See Fig. 13).

For incident K^- momenta smaller than 200 MeV/c, the maximum invariant mass of $\pi\Sigma$ in the $K^-d \rightarrow \pi\Sigma n$ reaction approaches that of the $\Lambda(1405)$ and the signal for this resonance becomes unclear. Thus, it is hard to investigate the $\Lambda(1405)$ properties in this reaction with incident K^- momenta smaller than 200 MeV/c.

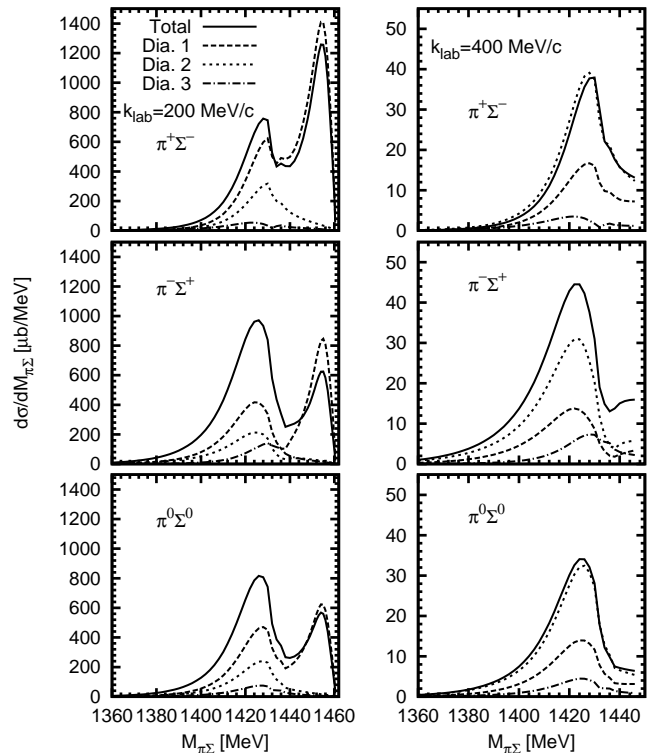


FIG. 12: $\pi\Sigma$ invariant mass spectra of $K^-d \rightarrow \pi\Sigma n$ separately plotted in each diagram contribution. The plots in the left and right panels are calculated with 200 and 400 MeV/c of K^- incident momenta, respectively. Same as described in the caption to Fig. 9.

IV. SUMMARY

We have studied the K^- induced production of $\Lambda(1405)$ with a deuteron target by calculating the observable $K^-d \rightarrow \pi\Sigma n$ reaction. We have found that, in the $K^-d \rightarrow \pi\Sigma n$ process, the $\Lambda(1405)$ resonance is produced by the $\bar{K}N$ channel, and, therefore, this process is suited to investigate the properties of the $\Lambda(1405)$ induced by subthreshold $\bar{K}N$.

We have calculated the $\pi\Sigma$ invariant mass spectra of the $K^-d \rightarrow \pi\Sigma n$ reaction using the $\bar{K}N \rightarrow \bar{K}N$ and $\bar{K}N \rightarrow \pi\Sigma$ amplitudes obtained by the chiral unitary approach. The present calculation agrees with the observed spectrum of $K^-d \rightarrow \pi^+\Sigma^-n$ in the bubble chamber experiment, in which the $\Lambda(1405)$ resonance appears at 1420 MeV not 1405 MeV. The present model also reproduces the $\Lambda(1405)$ production cross section. We have also found that the $\Lambda(1405)$ production has a strong angular dependence in this reaction and that the $\Lambda(1405)$ is produced mostly in backward directions against the incident K^- . We have shown that the production cross section decreases as the incident K^- momentum increases. Due to the worse momentum matching between the kaon and the nucleon inside the deuteron, the more energetic in-

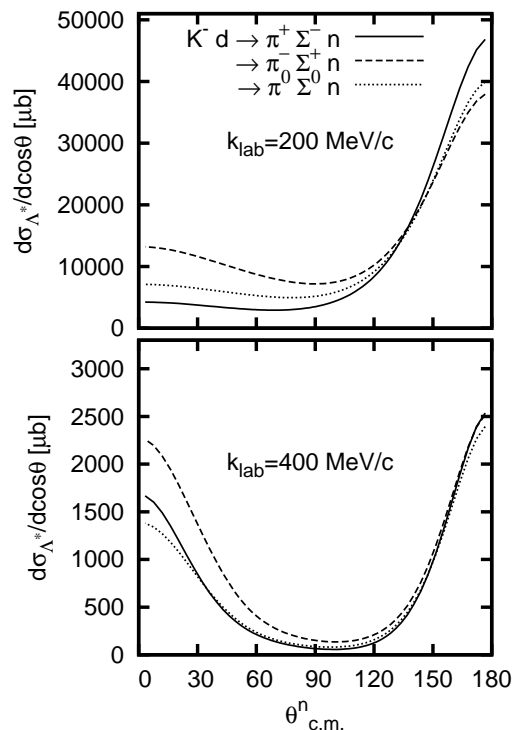


FIG. 13: Angular dependence of the $\Lambda(1405)$ production cross section for the incident K^- momenta of 200 MeV/c and 400 MeV/c in the upper and lower panels, respectively. Same as described in the caption to Fig. 10.

cident K^- s produce less $\Lambda(1405)$ s. These findings should be a guideline for future experiments that would help understand the dynamics and repercussions of subthreshold $\bar{K}N$ production of the $\Lambda(1405)$.

Acknowledgements

This work was partly supported by the Grant-in-Aid for Scientific Research from MEXT and JSPS (Nos. 20028004 and 20540273), the collaboration agreement between the JSPS of Japan and the CSIC of Spain, and the Grant-in-Aid for the Global COE Program "The Next Generation of Physics, Spun from Universality and Emergence" from MEXT of Japan. This work was also supported in part by DGICYT contract number FIS2006-03438. We acknowledge the support of the European Community-Research Infrastructure Integrating Activity "Study of Strongly Interacting Matter" (acronym HadronPhysics2, Grant Agreement n. 227431) under the Seventh Framework Programme of EU. Work supported in part by DFG (SFB/TR 16, "Subnuclear Structure of Matter"). This work was done under the Yukawa International Program for Quark-hadron Sciences (YIPQS).

-
- [1] R. H. Dalitz, T. C. Wong and G. Rajasekaran, Phys. Rev. **153**, 1617 (1967).
 - [2] N. Kaiser, P. B. Siegel, and W. Weise, Nucl. Phys. **A594**, 325 (1995).
 - [3] E. Oset and A. Ramos, Nucl. Phys. **A635**, 99 (1998).
 - [4] J. A. Oller and U. G. Meissner, Phys. Lett. **B500**, 263 (2001).
 - [5] E. Oset, A. Ramos, and C. Bennhold, Phys. Lett. **B527**, 99 (2002).
 - [6] C. Garcia-Recio, J. Nieves, E. Ruiz Arriola and M. J. Vicente Vacas, Phys. Rev. D **67**, 076009 (2003).
 - [7] T. Hyodo, S. I. Nam, D. Jido, and A. Hosaka, Phys. Rev. C **68**, 018201 (2003); Prog. Theor. Phys. **112**, 73 (2004).
 - [8] T. Hyodo, D. Jido and A. Hosaka, Phys. Rev. C **78**, 025203 (2008).
 - [9] D. Jido, J. A. Oller, E. Oset, A. Ramos and U. G. Meissner, Nucl. Phys. A **725**, 181 (2003).
 - [10] T. Hyodo, A. Hosaka, M. J. Vicente Vacas and E. Oset, Phys. Lett. B **593**, 75 (2004).
 - [11] J. C. Nacher, E. Oset, H. Toki and A. Ramos, Phys. Lett. B **461**, 299 (1999).
 - [12] S. Prakhov *et al.* [Crystall Ball Collaboration], Phys. Rev. C **70**, 034605 (2004).
 - [13] V. K. Magas, E. Oset and A. Ramos, Phys. Rev. Lett. **95**, 052301 (2005).
 - [14] C. Amsler *et al.* [Particle Data Group], Phys. Lett. B **667**, 1 (2008).
 - [15] M. Lacombe, B. Loiseau, R. Vinh Mau, J. Cote, P. Pires and R. de Tourreil, Phys. Lett. B **101**, 139 (1981).
 - [16] R. Machleidt, Phys. Rev. C **63**, 024001 (2001) [arXiv:nucl-th/0006014].
 - [17] D. N. Tovee *et al.*, Nucl. Phys. B **33**, 493 (1971); R. J. Nowak *et al.*, *ibid.* **139**, 61 (1978).
 - [18] R. J. Hemingway, Nucl. Phys. B **253**, 742 (1985).
 - [19] J. C. Nacher, E. Oset, H. Toki and A. Ramos, Phys. Lett. B **455**, 55 (1999).
 - [20] T. Hyodo and W. Weise, Phys. Rev. C **77**, 035204 (2008).
 - [21] O. Braun *et al.*, Nucl. Phys. B **129**, 1 (1977).